山西大学学报（自然科学版）48(4)：793－805，2025
Journal of Shanxi University(Nat. Sci. Ed.)

DOI：10.13451/j.sxu.ns.2024107

金纳米棒在近红外二区光声成像引导肿瘤光热治疗中的应用

王如意[1]，邢洋[1]，范博[1*]，张瑞平[2*]
（1.山西医科大学 药学院，山西 太原 030001；
2.山西医科大学附属医院山西省人民医院 放射科，山西 太原 030001）

摘　要：近红外二(the Second Near-infrared II，NIR-II)区光声(Photoacoustic，PA)成像引导光热治疗(Photothermal Therapy，PTT)具有增强穿透深度和提高信号强度等优势而备受关注。该方法可实现实时肿瘤诊断和原位治疗，在临床应用中具有显著优势。因此，迫切需要开发在NIR-II区具有临床转化潜力的光热材料。本文采用种子生长法制备了在NIR-II区具有强吸收的金纳米棒(Gold Nanorods，GNRs)，用于PA成像引导下的PTT研究。GNRs的光热转换效率高达36.68%，光热稳定性好。修饰后的聚乙二醇-金纳米棒(Polyethylene Glycol-Gold Nanorods，GNRs-PEG)，其细胞毒性较低，对小鼠乳腺癌细胞(4T1)细胞具有光热消融作用。建立原位乳腺癌模型，GNRs-PEG在4T1荷瘤小鼠体内具有良好光热治疗作用。此外，体内实验结果证明了GNRs-PEG通过PA成像引导的NIR-II区PTT消除肿瘤具有良好的治疗效果。本研究合成的GNRs-PEG作为NIR-II PA造影剂，在成像引导下的癌症治疗中具有广泛的应用前景。

关键词：聚乙二醇修饰金纳米棒；近红外二区；成像引导治疗
中图分类号：O69　　**文献标志码**：A　　**文章编号**：0253-2395(2025)04-0793-13

Gold Nanorods for Photoacoustic Imaging-guided Tumor Photothermal Therapy in the Second Near-infrared Region

WANG Ruyi[1], XING Yang[1], FAN Bo[1*], ZHANG Ruiping[2*]
(1. *School of Pharmacy, Shanxi Medical University, Taiyuan* 030001*, China;*
2. *The Radiology Department of Shanxi Provincial People' Hospital, Shanxi Medical University, Taiyuan* 030001*, China*)

Abstract: Photoacoustic (PA) imaging-guided photothermal therapy (PTT) in the second near-infrared (NIR-II) region has garnered increasing attention due to its inherent advantages, such as enhanced penetration depth and heightened signal intensity. This approach enables real-time tumor diagnosis and *in-situ* treatment simultaneously, offering significant advantages in clinical translation. Nevertheless, there is an urgent need for the development of photothermal agents with clinical translational potential in the NIR-II region. Here, we successfully synthesized gold nanorods (GNRs) exhibiting strong absorption in the NIR-II region, which enables precise PA imaging-guided PTT. GNRs has a high photothermal conversion efficiency of 36.68% and good photothermal stability. After being modified with polyethylene glycol (PEG), *in vitro* experiments showed that GNRs-PEG had ignorable cytotoxicity and showed efficient ablation of 4T1 cells. An orthotopic breast cancer model was established to study the *in vivo* anti-tumor efficacy of GNRs-PEG on 4T1 tumor-bearing mice. The results showed that GNRs-PEG had an enhanced tumor inhibitory effect. Additionally, *in vivo* PA imaging can be used to track the dynamic distribution of GNRs-PEG at the tumor site. Furthermore, *in vivo* results demonstrated the high effectiveness of GNRs-PEG for tumor elimination through PA imaging-guided PTT in the NIR-II region. In conclu-

收稿日期：2024-04-30；**接受日期**：2024-06-14
基金项目：国家重点研发计划(2023YFC3402800)；国家自然科学基金(82071987)
作者简介：王如意(1999—)，山西阳泉人，硕士，研究方向为纳米材料成像和药物递送研究。E-mail：727139971@qq.com
* **通信作者**：范博(FAN Bo)，E-mail：ty-fanbo@163.com；张瑞平(ZHANG Ruiping)，E-mail：zrp_7142@sxmu.edu.cn
引文格式：王如意，邢洋，范博，等.金纳米棒在近红外二区光声成像引导肿瘤光热治疗中的应用[J].山西大学学报(自然科学版)，2025，48(4)：793-805. DOI：10.13451/j.sxu.ns.2024107.

sion, the GNRs-PEG synthesized in this work hold broad applications as NIR-II PA contrast agents for imaging-guided cancer therapy.
Key words: polyethylene glycol modified gold nanorods; the second near-infrared region; image-guided therapy

1 Introduction

Due to its high morbidity and mortality rates worldwide, cancer poses a serious threat to human survival and quality of life[1]. Rapid, accurate diagnosis and effective treatment options are still lacking for cancers that require ongoing progression[2-3]. Diagnostic imaging modalities currently available include computed tomography (CT), magnetic resonance imaging (MRI), and X-ray[4]. However, these imaging techniques have some disadvantages, such as poor spatial resolution, low soft tissue contrast, long signal acquisition time, and radiation exposure[5]. Photoacoustic (PA) imaging represents a novel non-invasive molecular imaging technique that merges the high contrast of optical imaging with the deep penetration of ultrasound imaging, thereby facilitating its widespread application in biomedical disease diagnosis and functional imaging[6-7]. In comparison to the first near-infrared region (NIR-I, 650-900 nm), PA imaging within the second near-infrared region (NIR-II, 1 000-1 700 nm) not only affords a notably enhanced depth of penetration but also allows for a higher maximum permissible irradiation level owing to reduced absorption and scattering by skin tissues[8-9]. Meanwhile, the diminished background signal of the NIR-II region significantly enhances the imaging resolution. This feature positions NIR-II imaging as a promising and novel strategy for early cancer diagnosis and real-time monitoring of the treatment process[10-11].

In photothermal therapy (PTT), a photothermal agent (PTA) absorbs NIR laser light of a specific wavelength and converts light energy into heat. Excessive heat can induce apoptosis or necrosis of tumor cells, thus causing damage to tumor tissues[12]. More importantly, the external laser light source can selectively irradiate the tumor site, thereby substantially reducing the potential damage to normal tissues during treatment[13]. This is especially suitable for the treatment of tumors at the superficial anatomical locations. Breast cancer is a superficial tumor where light can penetrate the normal tissue to reach the focus, enabling specifically targeted therapy. Specifically, PA imaging-guided PTT could track the distribution of PTA in focus and provide appropriate timing for photothermal treatment[14-15].

At present, various materials have been developed and applied in phototheranostics research, including noble metals[16], semiconductors[17], and carbon materials[18]. The pivotal issue lies in the development of PTAs with clinical translational prospects. Gold nanomaterials have received much attention due to their tunable absorption resonance peak, excellent photostability, high photothermal conversion efficiency, and promising prospects in clinical applications[19]. Notably, gold nanoparticles have received FDA approval for cancer treatment in clinical trials[20]. In addition, Au@silica nanoshells have been utilized for thermotherapy, securing FDA approval in 2012 (NCT01270139)[21]. These achievements underscore the potential of gold nanomaterials in advancing cancer therapy toward clinical translation. However, the majority of PTAs have been reported within the NIR-I region[22]. Among various gold nanomaterials, gold nanorods (GNRs) can range in size, and the wavelength of the SPR can be precisely tuned in the visible and NIR regions as the aspect ratio changes[23-24]. Because GNRs have the characteristics of a strong absorption band in the NIR-II region and photothermal conversion efficiency, GNRs have become candidate products for PTAs[25]. Cetyltrimethyl ammonium bromide (CTAB) was the most common surfactant for GNR synthesis. However, the incorporation of CTAB resulted in a significant positive charge on the surface of nanoparticles, leading to obvious biotoxicity of GNRs[26]. In addressing this problem,

polymers[27], natural polymeric materials[28-29], silica[30], and graphene[31] have been applied to exchange and/or block the original CTAB on the surface of GNRs, thereby rendering it suitable for utilization in studies related to PTT. Up to now, several types of GNRs absorbed in the NIR-II region, such as hollow GNRs[19] or substances coated to the surface of GNRs[32], have been explored as PA contrast agents for PA imaging-guided PTT. In contrast, superhigh aspect ratios GNRs are relatively simple to prepare and exhibits exceptional photothermal conversion efficiency, rendering them highly suitable for NIR-II PA image-guided PTT.

In this study, GNRs with strong absorption at 1 064 nm in the NIR-II region were synthesized and employed for PA imaging-guided PTT of tumors (Scheme 1). The NH_2-PEG-SH was modified on the surface of GNRs through S—Au covalent bonding[33]. After being modified with polyethylene glycol (PEG), a hydrophilic and flexible polymer, GNRs-PEG displayed reduced cytotoxicity and decreased protein adsorption on the surface, thus avoiding recognition by the immune system and prolonging circulation time[34]. The GNRs-PEG showed good biocompatibility, high photothermal stability, and a photothermal conversion efficiency of 36.68%. Furthermore, NIR-II lasers (1 064 nm, 100 mJ/cm^2) permit a significantly higher maximum permissible exposure (MPE) compared to NIR-I lasers (808 nm, 33 mJ/cm^2), thereby enabling higher laser power for enhancing PA imaging performance[35-36]. In vivo, diagnosis and treatment outcomes confirm that GNRs-PEG can serve as a viable candidate for tumor treatment through PA imaging-guided PTT.

2 Materials and methods

2.1 Materials

Gold (III) chloride hydrate ($HAuCl_4$, 99%), hydroquinone, and fluorescein isothiocyanate (FITC) were obtained from Macklin (Shanghai, China). Cetyltrimethylammonium bromide (CTAB, AR), sodium hydroxide (NaOH, AR), sodium borohydride ($NaBH_4$, AR), and silver nitrate ($AgNO_3$, AR) were acquired from Tianjin Kaitong Chemical Reagent Co. LTD. NH2-PEG-SH (M. W. 5000 Da) was provided from Guangzhou Weihua Biotechnology Co. LTD. The Cell Counting Kit-8 (CCK-8) and 4', 6-diamidino-2-phenylindole (DAPI) were obtained from

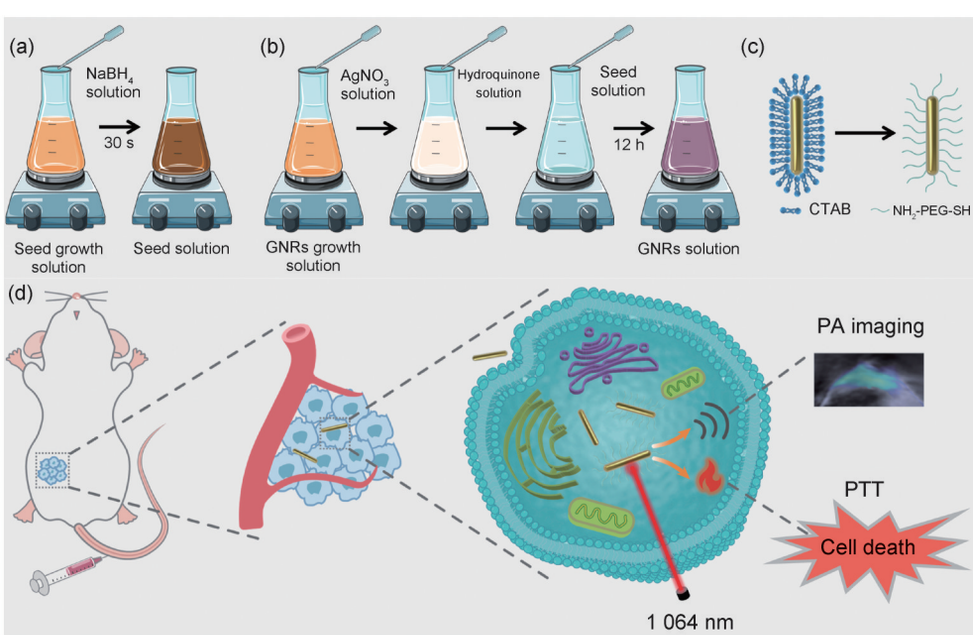

Scheme 1 Schematic representation of GNRs-PEG with strong absorption in the NIR-II region for tumor PTT guided by PA imaging. (a) Synthesis of seed solutions. (b) Synthesis of GNRs. (c) PEG modification of GNRs. (d) Schematic representation of GNRs-PEG acting in vivo

Saiwen Innovation Biotechnology Co., Ltd. (Beijing, China).

2.2 Synthesis of GNRs-PEG

Gold seed solution was synthesized following previously described methods[37]. Briefly, $HAuCl_4$ solution (0.001 mol/L) and CTAB (0.2 mol/L) were combined in a volume ratio of 1∶1, and an appropriate amount of ice-cold $NaBH_4$ (0.01 mol/L) was rapidly added under vigorous stirring for 30 s. Age the seed solution for 5 min at room temperature. Afterward, 5 mL of $HAuCl_4$ (0.001 mol/L) and 5 mL of CTAB (0.2 mol/L) were mixed. Then, 105 μL of $AgNO_3$ solution and 400 μL of hydroquinone solution at an equal concentration (0.1 mol/L) were added. Subsequently, 75 μL of gold seed solution was added and the reaction was allowed to proceed for 12 hours at 30 ℃. The obtained GNRs were collected by centrifugation at 8 000 g for 30 minutes and washed with water.

To reduce toxicity and increase the long circulation of GNRs, GNRs were mixed with NH_2-PEG-SH at a mass ratio of 1∶10 and reacted overnight. Finally, the GNRs-PEG was washed with water and harvested through centrifugation.

2.3 Characterization of GNRs-PEG

The morphology of GNRs was observed by TEM. The size and zeta potential were measured using Zatesizer Nano ZS90 (Malvern Instruments Ltd., Malvern, UK). The optical properties were studied using the UV-vis-NIR absorption spectra. Additionally, the GNRs and GNRs-PEG were examined with FT-IR spectroscopy.

2.4 Photothermal property of GNRs-PEG

Different concentrations of GNRs-PEG dispersions (0, 25, 50, 75, 100, 125 and 150 μg/mL) were irradiated with a NIR-Ⅱ laser (1 064 nm, 1.0 W/cm^2) for 5 min. Furthermore, 100 μg/mL of GNRs-PEG dispersion was irradiated with a 1 064 nm laser for 5 min at different power (0.25, 0.5, 1.0, 1.25, and 1.5 W/cm^2). The temperature changes were recorded at 10-second intervals using an infrared thermal camera (Fluke Ti 400). To assess the photothermal stability, the GNRs-PEG dispersion (100 μg/mL) was irradiated for 5 min using 1.0 W/cm^2 laser, followed by naturally cooled to the initial temperature. This ON-OFF cycle of laser irradiation was repeated five times.

The GNRs-PEG dispersion was exposed to 1 064 nm irradiation (1.0 W/cm^2, 5 min). Subsequently, turn off the laser and allow the solution to cool naturally. The relationship between temperature and time was recorded and then calculation of thermal conversion efficiency.

2.5 Cell and culture

4T1 cells were maintained in a complete DMEM medium supplemented with 10% FBS containing 1.0% penicillin-streptomycin, and cultured in a stable environment of 5.0% CO_2 at 37 ℃. All cell experiments were conducted during the logarithmic phase of cell growth in optimal conditions.

2.6 Cytotoxicity of GNRs-PEG

The CCK-8 assay was performed to evaluate cell viability. Briefly, 4T1 cells were seeded in 96-well plates until adherence. Subsequently, GNRs-PEG solution with various concentrations was added and incubated with 4T1 cells for 24 hours. Then, the solution was removed and cells were washed with PBS twice. Afterward, 100 μL of medium containing 10 μL of CCK-8 reagent was added into each well and incubated for 1 hour. Cell viability was evaluated by determining the absorbance at 450 nm using a microplate reader (Spectra Max Plus 384, Molecular Devices). The cell viability (CV, %) calculation formula was as follows:

$$\mathrm{CV}(\%)=\frac{A_{\mathrm{test}}}{A_{\mathrm{control}}}\times 100\%$$

2.7 Cellular uptake

To examine cellular uptake, fluorescently labeled GNRs-PEG was prepared. The GNRs-PEG solution was mixed with fluorescein isothiocyanate (FITC) at a ratio of 5∶1 in the dark for 2 h. GNRs-PEG-FITC were obtained by washing with deionized water. Subsequently, 4T1 cells were seeded in 6-well plates at a density of 3×10^5 cells per well. 24 hours later, GNRs-PEG-FITC solution (100 μg/mL) was add-

ed and incubated for different time points. Untreated cells were used as controls. Then, the cell suspension was collected, followed by resuspension in PBS. These procedures were performed in the dark. The fluorescence intensity of GNRs-PEG-FITC uptake by cells at different time points was assessed using flow cytometry (Navios, Beckman Coulter).

In addition, the cell colocalization experiment further verified the cellular uptake of GNRs-PEG. After 4T1 cells were seeded on the sterile glass slides and co-incubated with 100 μg/mL of GNRs-PEG-FITC solution for 8 h. Subsequently, the slides were carefully removed and the cell nuclei were stained with DAPI. Cells were imaged using confocal laser scanning microscopy (Fluoview FV3000, Olympus).

2.8 The anti-tumor experiment of GNRs-PEG in vitro

The in vitro therapeutic effect of GNRs-PEG was evaluated by in vitro proliferation inhibition assay. A density of 8×10^3 cells per well was seeded in 96-well plates. After adherence, cells were co-incubated with GNRs-PEG solution (100 μg/mL) for 4 hours, and then irradiated using a 1 064 nm laser (1.0 W/cm^2, 5 min). The PBS and non-irradiation groups were used as controls. The cells were then cultured for an additional 20 hours. Similarly, medium containing CCK-8 reagent was added into each well, followed by incubation of 1 h. The microplate reader (Spectra Max Plus384, Molecular Devices) was used to measure the cell proliferation viability by calculating the absorbance value at 450 nm.

Trypan blue staining was also performed on 4T1 cells to evaluate cell apoptosis. The 4T1 cells were stained for 5 min with Trypan Blue diluting solution (0.04%), and the cells of each group were cleaned with PBS, and photographed under an optical microscope.

2.9 PA imaging

To examine in vitro PA imaging effects, various concentrations of GNRs-PEG solution (0, 100, 150, 200, 250, 500 μg/mL) were placed in a polyurethane tube and imaged by a real-time multispectral optoacoustic tomography imaging system (MOST insight128, Germany). The PA signals were collected under the laser wavelength at 1 064 nm. Finally, the linear relationship between PA signals and the sample concentrations of GNRs-PEG was calculated.

GNRs-PEG solution (10 mg/kg) was injected into the 4T1 tumor-bearing mice via the tail vein for in vivo PA imaging. Then mice were imaged using the Vevo-LAZR-X high-frequency photoacoustic ultrasound imaging system for small animals, and the PA signal intensity was captured at different time intervals.

2.10 Photothermal performance of GNRs-PEG in vivo

The 4T1 tumor-bearing mice were randomly divided into two groups and intravenously injected with saline or GNRs-PEG (10 mg/kg), respectively. After 8 h post-injection, mice were irradiated with the 1 064 nm laser (1.0 W/cm^2, 5 min). The body temperature of mice during photothermal treatment was monitored using an infrared thermal camera.

2.11 Anti-tumor efficacy after PTT in vivo

The 4T1 tumor-bearing mice were randomly divided into four groups (Saline, Saline+Laser, GNRs-PEG, and GNRs-PEG+Laser). The GNRs-PEG (10 mg/kg) were then intravenously administrated into mice. The Laser group was irradiated through a 1 064 nm laser (1.0 W/cm^2, 5 min) after 8 hours of administration. The temperature of mice was monitored during photothermal treatment. The tumor volumes and body weight were recorded every other day for 14 days.

2.12 Histological analysis and blood biochemistry

After the treatment, H&E staining of the major tissue organs (heart, liver, spleen, lungs, and kidneys) was performed. TUNEL staining was carried out using commercially available kits (DAB (SA-HRP) Tunel Cell Apoptosis Detection). To preliminarily assess the in vivo toxicity, the whole blood and serum of mice were collected to detect the biochemical indicators.

3 Results and discussion

3.1 Characterization of GNRs

The GNRs were synthesized using the seed-mediated method, which had been optimized in previous studies. As shown in Fig. 1(a) and 1(b), the TEM result revealed that the GNRs had a stable and uniform rod-like morphology with an average length and width of 84.25 nm and 13.02 nm, respectively. Importantly, the SPR wavelength of GNRs could be varied with the aspect ratio[38]. The obtained GNR aspect ratio was about 6.4∶1 and had a strong absorbance in the NIR-II region (Fig. 1(c)), indicating the potential for PTT and PA imaging. After modified the PEG, the zeta potential was +30 mV for bare GNRs and was decreased to +10 mV after PEG modification. FT-IR spectroscopy was used to analyze the successful preparation of NH_2-PEG-SH and GNRs-PEG. As shown in Fig. 1(d), the S-H stretching band of GNRs-PEG disappeared at 2 691 cm^{-1}, indicating the successful modification of NH2-PEG-SH on the surface of GNRs.

3.2 Photothermal performance of GNRs-PEG

The GNRs-PEG dispersions with different concentrations were irradiated with a 1 064 nm laser. The results of thermal images showed that increasing the concentration of nanomaterials and the duration of laser exposure could enhance the photothermal performance of GNRs-PEG (Fig. 2(a) and 2(b)). In contrast, the temperature of pure water was almost unchanged under the same conditions. Meanwhile, 100 μg/mL of GNRs-PEG dispersion was irradiated by laser at 1 064 nm for 5 min, when the irradiation power was increased from 0.5 W/cm^2 to 1.5 W/cm^2, the dispersion temperature was increased from 33.2 ℃ to 63.9 ℃ (Fig. 2(c) and Fig. S1). These results showed that GNRs-PEG could efficiently converts light to heat and probably serve as a good PTAs. In addition, the photothermal stability of GNRs-PEG was investigated by a heating-cooling cycle experiment. The 100 μg/mL of GNRs-PEG was subjected to five consecutive ON-OFF cycles at a power of 1.0 W/cm^2

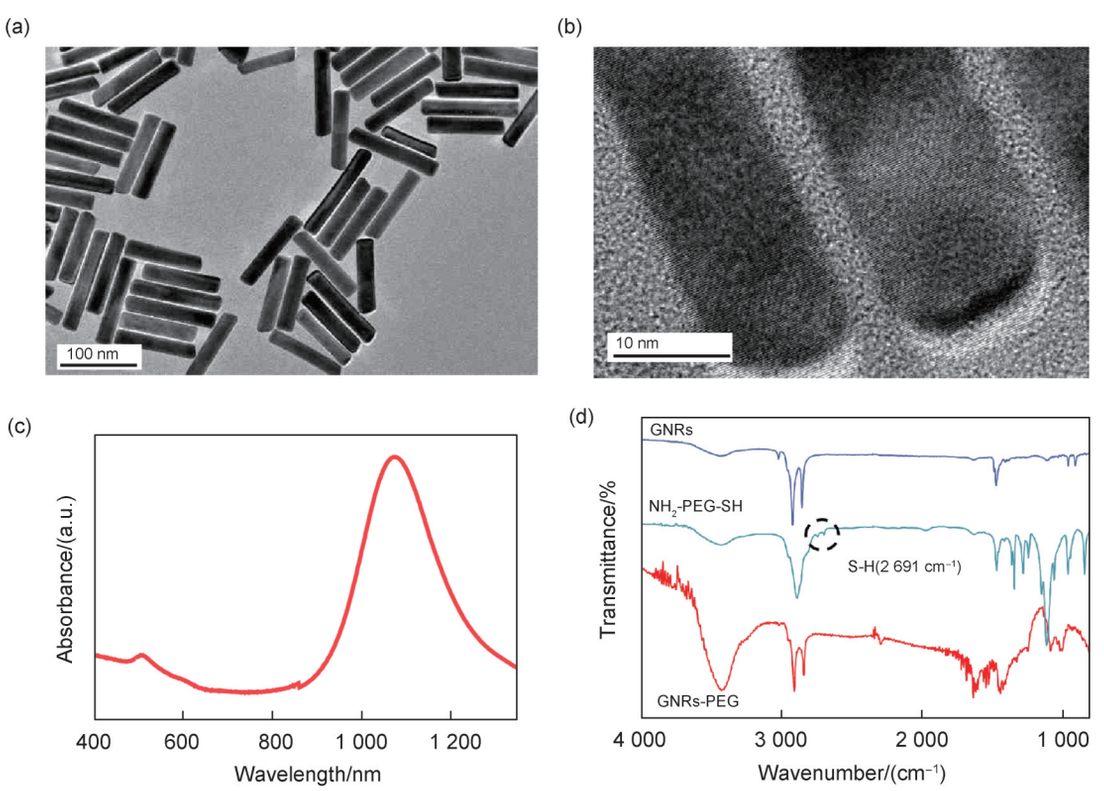

Fig. 1 Characterization of GNRs

(a) TEM images of GNRs, scale bar = 100 nm; (b) TEM images of GNRs, scale bar = 10 nm; (c) UV-vis-NIR spectra of GNRs; (d) FT-IR spectra of GNRs, NH_2-PEG-SH and GNRs-PEG

(Fig. 2(d)). The maximum temperature of each cycle remained constant and the duration of each set of cycles was almost the same, which indicated that the GNRs had good photothermal stability. Furthermore, the photothermal conversion efficiency of the GNRs−PEG was 36.68% by fitting the curve of average temperature over time (Fig. 2(e) and 2(f), Supporting information). Such high values indicated the great potential of GNRs−PEG to be used as PTT and PA contrast agents.

3.3 Cell assay

The CCK-8 method was used to evaluate the toxicity of GNRs−PEG on 4T1 cells. After co−incubation with different concentrations, the survival rates of 4T1 cells were above 80% within the study concentration range (Fig. 3(a)). The results indicated the good biocompatibility of GNRs−PEG for biomedical applications.

The cell uptake of GNRs−PEG−FITC was detected by flow cytometry. As illustration in Fig. 3(b) and 3(c), the fluorescence intensity gradually increased with the prolongation of the co−incubation time. The fluorescence intensity peaked at 8 h, indicating that the cells had completed the uptake of GNRs-PEG. Meanwhile, confocal laser scanning images showed that the green fluorescence was local-

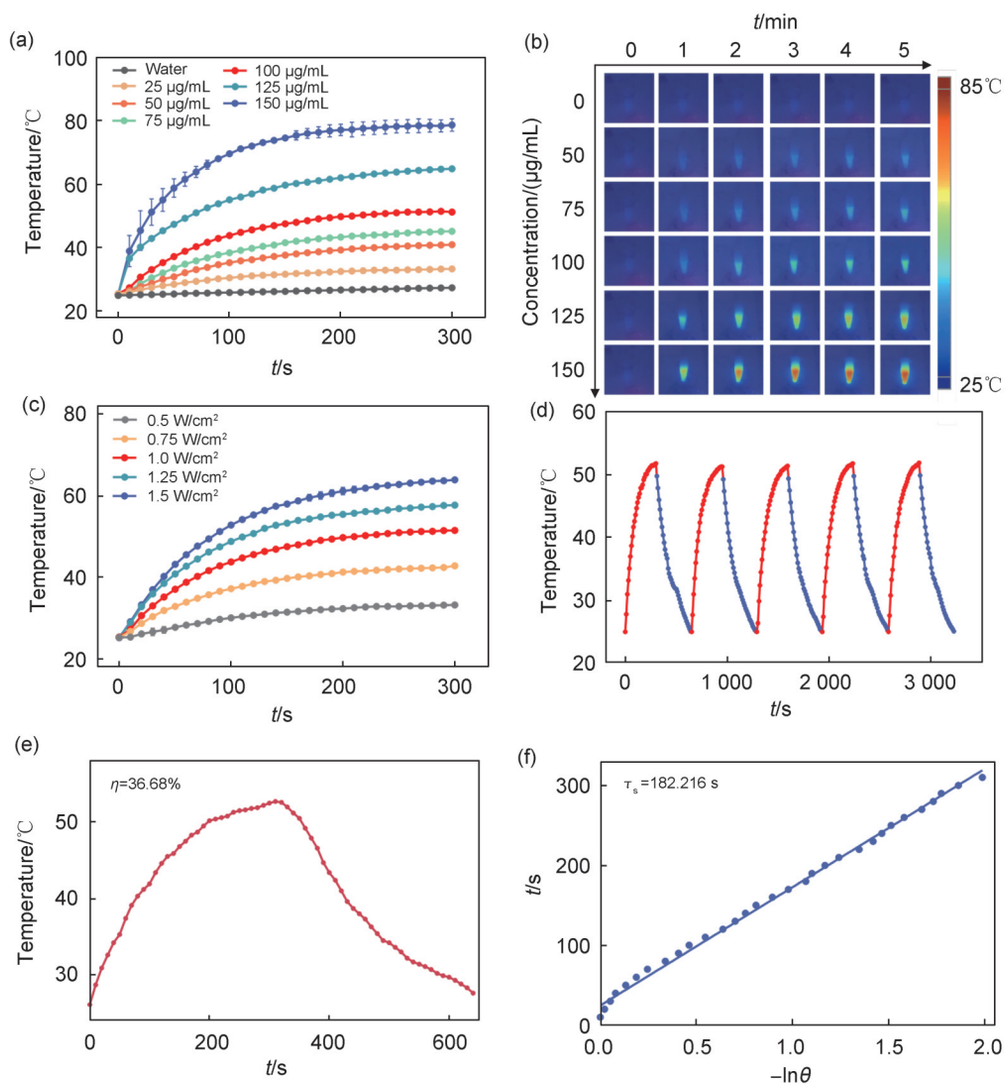

Fig. 2 Photothermal properties of GNRs-PEG

(a) Temperature increase curves of GNRs-PEG with different concentration; (b) the corresponding thermal image; (c) temperature increase curves of GNRs-PEG with different power; (d) photothermal stability of GNRs-PEG; (e) heating/cooling curve; (f) the plot of cooling time versus negative natural logarithm of the temperature driving force obtained from cooling stage

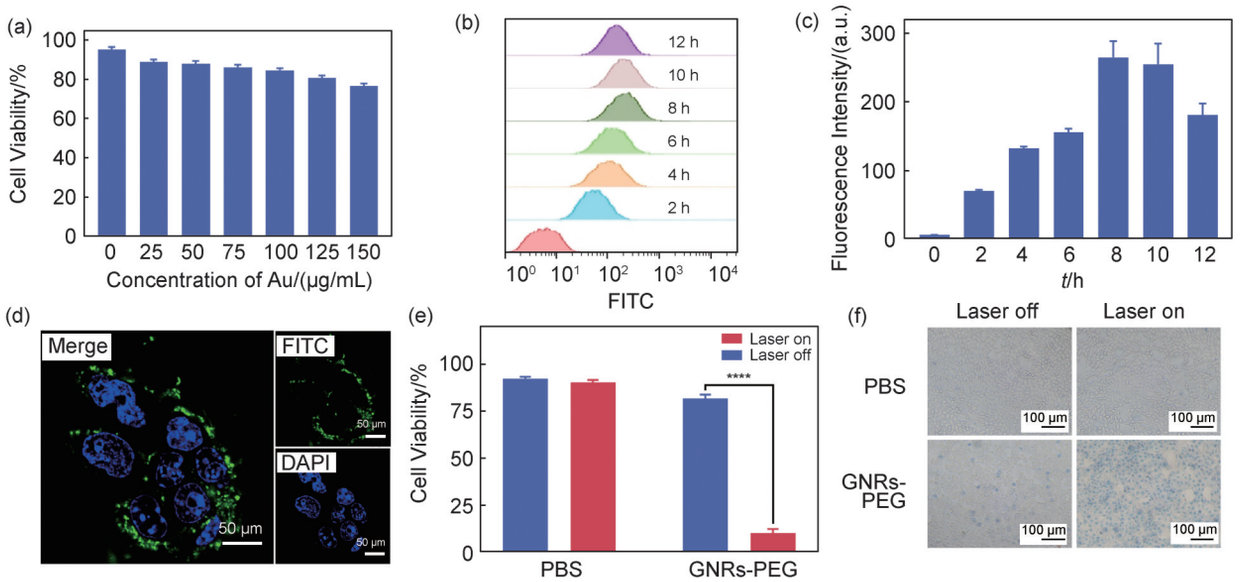

Fig. 3 Antitumor effects of GNRs-PEG *in vitro*

(a) Cell viability of 4T1 cells treated with various concentrations of GNRs-PEG; (b) intracellular uptake of GNRs-PEG in 4T1 cells at different time points detected by flow cytometer; (c) the corresponding statistical analysis; (d) uptake images of GNRs-PEG-FITC by 4T1 cells at 8 h *via* CLSM (scale bar = 50 μm); (e) 4T1 cells treated with/without 1 064 nm irradiation (****$p < 0.001$); (f) trypan blue staining of 4T1 cells by GNRs-PEG under laser irradiation/non-irradiation, scale=100 μm

ized in the cytoplasm after 8 h incubation of GNRs−PEG (Fig. 3(d)). These results indicated that 4T1 cells could effectively uptake GNRs−PEG.

In addition, the photothermal anti-tumor effect of GNRs−PEG was detected by the CCK−8 method. The cell survival rate in the PBS group was high (>90%) with or without laser irradiation. In contrast, the cell survival rate was lower than 12% in 4T1 cells after incubation with 100 μg/mL of GNRs−PEG pulse laser irradiation (Fig. 3(e)). These results confirmed that GNRs−PEG could effectively kill tumor cells under NIR-II laser irradiation.

The viability of 4T1 cells was assessed using Trypan blue staining. Trypan blue staining enables a rapid and straightforward differentiation between live and dead cells. Normal viable cells with intact membrane structures prevent the entry of Trypan blue. Conversely, cells exhibiting reduced activity or compromised cell membranes display increased permeability and can be stained blue by Trypan blue. Loss of cell membrane integrity indicates cellular death. As depicted in Fig. 3(f), laser irradiation had minimal impact on the survival of PBS-treated cells, with only a few deceased cells observed within the visual field. GNRs−PEG treatment also did not impede cell growth. However, upon laser irradiation in the GNRs−PEG group, an abundance of blue regions and an increased number of dead cells were evident under microscopic examination. These experimental findings demonstrate that GNRs−PEG can effectively induce tumor cell death through photothermal action when exposed to laser irradiation.

3.4 PA imaging of GNRs−PEG

PA signals of GNRs-PEG solutions at various concentrations were measured using a photoacoustic system (Fig. 4(a)). As the concentration of GNRs−PEG increased, the intensity of the PA signal gradually enhanced. In addition, there was a linear correlation between the photoacoustic signal and concentration in the range of 0 to 500 μg/mL.

PA imaging of GNRs−PEG as an exogenous contrast agent in 4T1 tumor-bearing mice was studied. The PA signals were acquired at appropriate time intervals after injection of GNRs−PEG (10 mg/kg) in tumor−bearing mice. Ultrasound (US) and PA images of tumor-bearing mice at different time was depicted in Fig. 4(b). The PA signals of tumor tissues reached the maximum at 8 h post-injection. It indi-

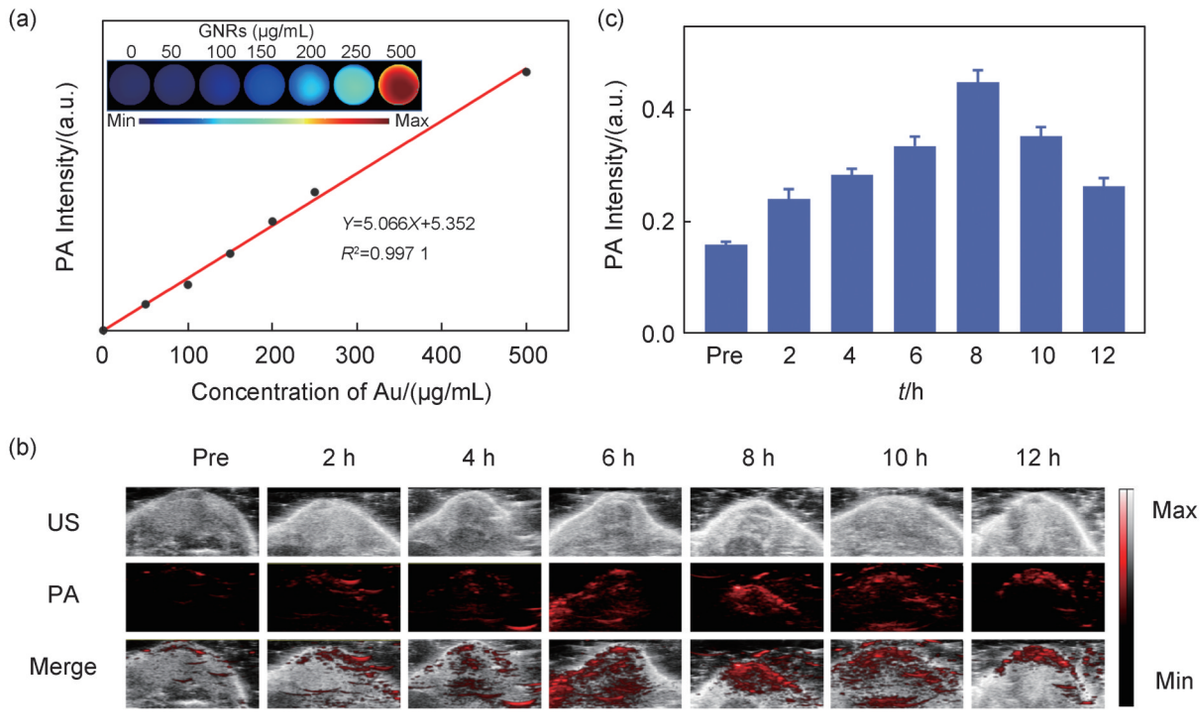

Fig. 4 **PA** imaging of GNRs-PEG

(a) PA images and signal intensity of GNRs-PEG with different concentrations; (b) US and PA images of tumor-bearing mice at different time; (c) quantitative analysis

cated that GNRs−PEG accumulates most in the tumor at 8 h post−injection, and was eliminated from the body after 12 h (Fig. 4(c)).

3.5 Anti−tumor effect of GNRs−PEG in vivo

The in vivo anti−tumor efficacy of GNRs−PEG in 4T1 tumor−bearing mice, guided by PA imaging, was further investigated. The experimental procedure was depicted in Fig. 5(a). 4T1 tumor−bearing mice were randomly divided into four groups: saline, saline＋Laser, GNRs−PEG, and GNRs−PEG＋Laser. According to the maximum enrichment time shown in the PA images, mice in the Laser plus group received 1 064 nm laser irradiation (1.0 W/cm^2, 5 min) at 8 h post-administration. The temperature changes at the tumor site were recorded using a NIR thermal imaging camera (Fig. 5(b)). As depicted in Fig. 5(c), the temperature increased by 2.3 ℃ in the control and 12.8 ℃ in the GNRs−PEG group, respectively. This suggests that laser irradiation alone was insufficient to achieve the desired photothermal effect, whereas GNRs−PEG combined with laser treatment exhibited a robust hyperthermic effect on tumor tissues. These findings underscore the high photothermal efficiency of GNRs−PEG. Additionally, after 14 days, tumors in the GNRs−PEG and laser-treated group exhibited a size reduction. In contrast, tumors in all other groups exhibited significant growth, indicating that treatment with GNRs-PEG alone or laser irradiation alone failed to inhibit tumor growth (Fig. 5(d) and 5(e)). Throughout the entire experimental period, there was no significant change observed in the body weight of mice across all groups (Fig. 5(f)). Furthermore, the TUNEL assay demonstrated that the GNRs−PEG＋Laser induced a notable level of tumor apoptosis (Fig. 5(g)). These findings collectively affirm the remarkable PTT efficacy of GNRs−PEG, leading to complete tumor elimination in vivo.

3.6 Biological safety

Considering the *in vivo* biosafety of GNRs−PEG, histological examination using H&E staining of major organs and analysis of blood biochemical indicators were conducted. The results demonstrated no statistically significant differences between the GNRs−PEG and control groups (Fig. 6(a),

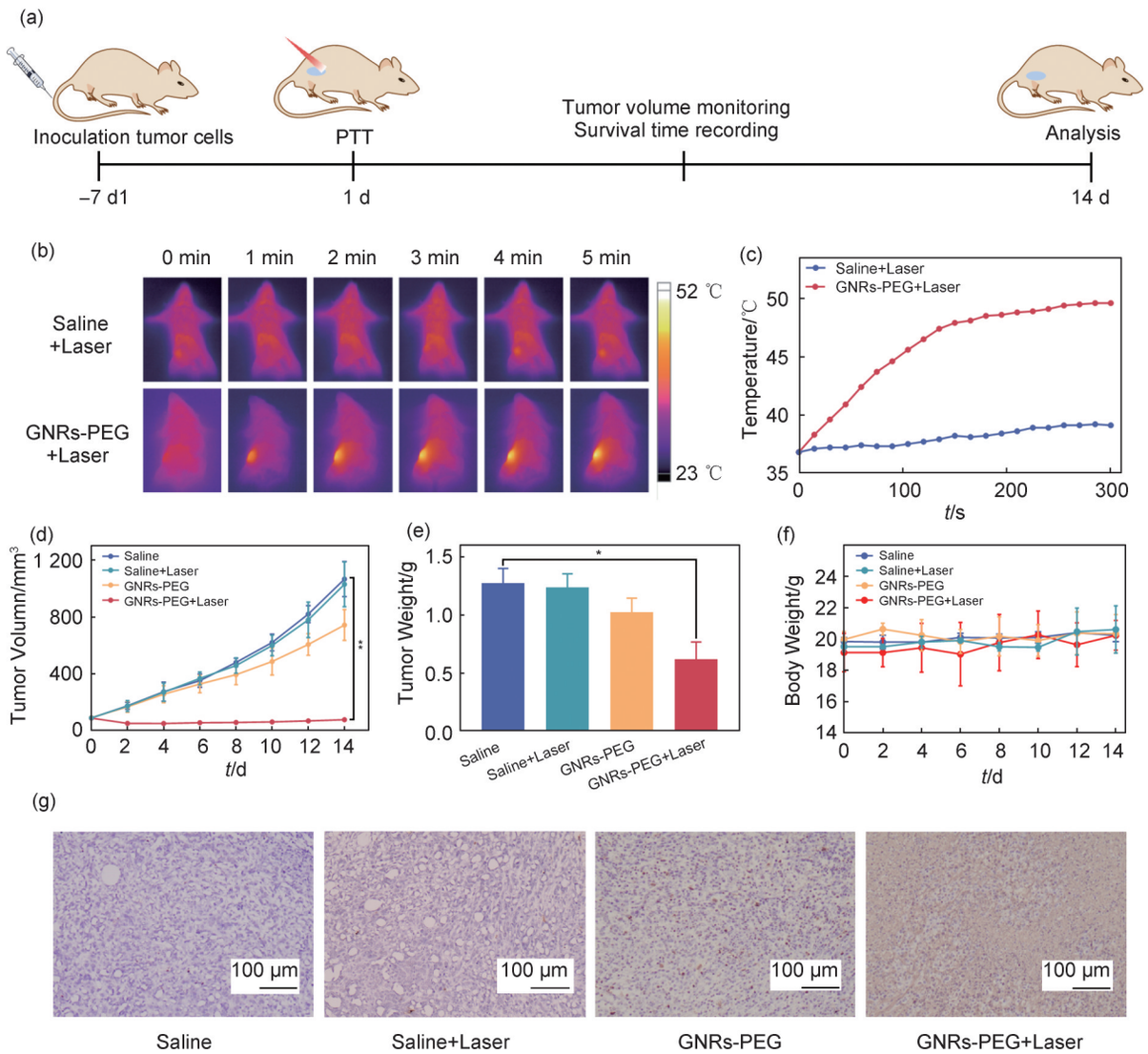

Fig. 5 Antitumor PTT effects of GNRs-PEG in vivo

(a) Schematic diagram showing the experimental approach; (b) infrared thermal images; (c) temperature change of Saline+Laser and GNRs-PEG+Laser group at predetermined time points; (d) the ralative tumor volumes curves; (e) weights of tumors (*p < 0. 05 and **p < 0. 01); (f) changes in the mice body weight through the 14 days treatment period; (g) histopathology evaluation of tumor tissues after TUNEL staining

6(b), indicating the favorable biosafety profile of GNRs−PEG. Thus, GNRs−PEG could be considered promising candidates for PA imaging-guided PTT.

4 Conclusion

In summary, GNRs with PA imaging and PTT characteristics in the NIR−II region were successfully synthesized using a seed−mediated method. Surface modification of GNRs with PEG significantly enhanced their biocompatibility. The GNRs−PEG demonstrated strong NIR−Ⅱ absorption and exhibited favorable characteristics including high stability and negligible toxicity. *In vivo* investigation revealed that GNRs−PEG accumulated specifically in the tumor region following intravenous administration, resulting in an augmented photothermal response. Furthermore, the tumors subjected to PTT under NIR−II PA imaging guidance demonstrated a substantial suppression of growth. These findings underscore the remarkable capabilities of GNRs−PEG for NIR−II PA imaging and their potential for image-guided tumor therapy.

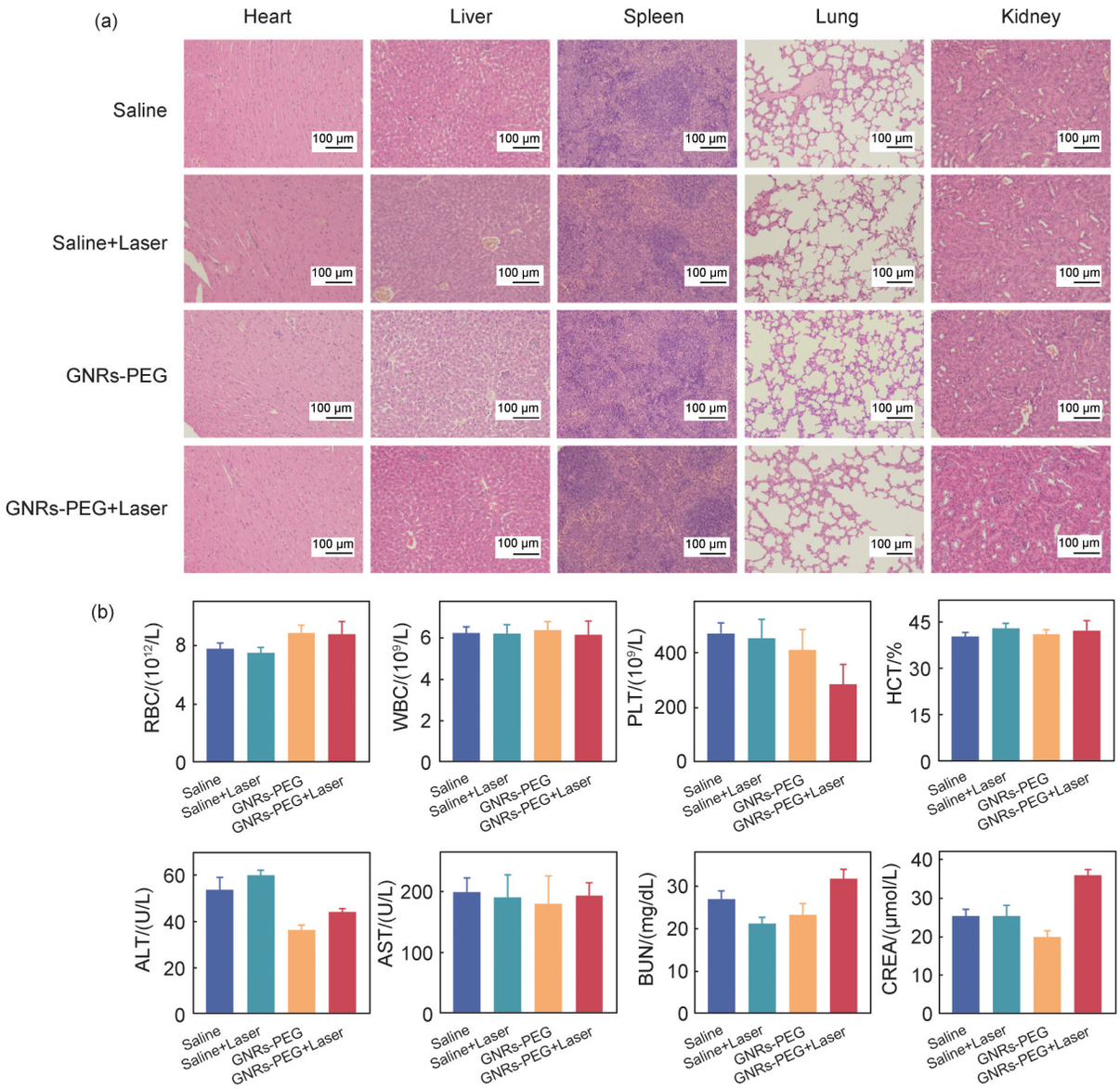

Fig. 6 Biological safety of GNRs-PEG

(a) Histopathology evaluation of major organ tissues after H&E staining. Scale bar = 100 μm; (b) Blood routine index (RBC, WBC, PLT and HCT) and chemistry indexes (ALT, AST, BUN and CREA) in different groups

References:

[1] JOST A, PFEIFER F. Interaction of the Gas Vesicle Proteins GvpA, GVPC, GVPN, and GvpO of *Halobacterium salinarum*[J]. *Front Microbiol*, 2022, **13**: 971917. DOI: 10.3389/fmicb.2022.971917.

[2] LU Y, HU X X, PANG J, *et al*. Parallel Reaction Monitoring Mass Spectrometry for Rapid and Accurate Identification of B-lactamases Produced by *Enterobacteriaceae* [J]. *Front Microbiol*, 2022, **13**: 784628. DOI: 10.3389/fmicb.2022.784628.

[3] SINDHWANI S, SYED A M, NGAI J, *et al*. The Entry of Nanoparticles into Solid Tumours[J]. *Nat Mater*, 2020, **19**(5): 566−575. DOI: 10.1038/s41563-019-0566-2.

[4] CAI Y, WEI Z, SONG C H, *et al*. Optical Nano-agents in the Second Near-infrared Window for Biomedical Applications[J]. *Chem Soc Rev*, 2019, **48**(1): 22−37. DOI: 10.1039/C8CS00494C.

[5] DEÁN-BEN X L, GOTTSCHALK S, LARNEY B M, *et al*. Advanced Optoacoustic Methods for Multiscale Imaging of in vivo Dynamics[J]. *Chem Soc Rev*, 2017, **46**(8): 2158−2198. DOI: 10.1039/c6cs00765a.

[6] FU Q R, ZHU R, SONG J B, *et al*. Photoacoustic Imaging: Contrast Agents and Their Biomedical Applications [J]. *Adv Mater*, 2019, **31**(6): e1805875. DOI: 10.1002/adma.201805875.

[7] BORUM R M, MOORE C, MANTRI Y, *et al*. Supramo-

lecular Loading of DNA Hydrogels with Dye-drug Conjugates for Real-time Photoacoustic Monitoring of Chemotherapy[J]. *Adv Sci*, 2022, **10**(1): e2204330. DOI: 10.1002/advs.202204330.

[8] LIU Y S, LI Y, KOO S, *et al*. Versatile Types of Inorganic/Organic NIR-IIa/IIb Fluorophores: From Strategic Design Toward Molecular Imaging and Theranostics[J]. *Chem Rev*, 2022, **122**(1): 209−268. DOI: 10.1021/acs.chemrev.1c00553.

[9] LI Z F, ZHANG C, ZHANG X, *et al*. NIR-II Functional Materials for Photoacoustic Theranostics[J]. *Bioconjug Chem*, 2022, **33**(1): 67−86. DOI: 10.1021/acs. bioconjchem.1c00520.

[10] PHILP L, CHAN H, ROUZBAHMAN M, *et al*. Use of Porphysomes to Detect Primary Tumour, Lymph Node Metastases, Intra-abdominal Metastases and as a Tool for Image-guided Lymphadenectomy: Proof of Concept in Endometrial Cancer[J]. *Theranostics*, 2019, **9**(9): 2727−2738. DOI: 10.7150/thno.31225.

[11] SUN J H, CAI W W, SUN Y, *et al*. Facile Synthesis of Melanin-dye Nanoagent for NIR-II Fluorescence/Photoacoustic Imaging-guided Photothermal Therapy[J]. *Int J Nanomedicine*, 2020, **15**: 10199−10213. DOI: 10.2147/IJN.S284520.

[12] ZHANG Y J, FENG Y Y, HUANG Y Q, *et al*. Tumor-targeted Gene Silencing IDO Synergizes PTT-induced Apoptosis and Enhances Anti-tumor Immunity[J]. *Front Immunol*, 2020, **11**: 968. DOI: 10.3389/fimmu.2020.00968.

[13] DUN X Y, LIU S L, GE N, *et al*. Photothermal Effects of CuS-BSA Nanoparticles on H22 Hepatoma-bearing Mice[J]. *Front Pharmacol*, 2022, **13**: 1029986. DOI: 10.3389/fphar.2022.1029986.

[14] LIU Y J, BHATTARAI P, DAI Z F, *et al*. Photothermal Therapy and Photoacoustic Imaging via Nanotheranostics in Fighting Cancer[J]. *Chem Soc Rev*, 2019, **48**(7): 2053−2108. DOI: 10.1039/c8cs00618k.

[15] RUAN X H, WEI M, HE X Y, *et al*. Asymmetric Aza-BODIPY Photosensitizer for Photoacoustic/Photothermal Imaging-guided Synergistic Photodynamic/Photothermal Therapy[J]. *Colloids Surf B Biointerfaces*, 2023, **231**: 113547. DOI: 10.1016/j.colsurfb.2023.113547.

[16] HAN H H, KIM S J, KIM J, *et al*. Bimetallic Hyaluronate-modified Au@Pt Nanoparticles for Noninvasive Photoacoustic Imaging and Photothermal Therapy of Skin Cancer [J]. *ACS Appl Mater Interfaces*, 2023, **15**(9): 11609−11620. DOI: 10.1021/acsami.3c01858.

[17] VAYALAKKARA R K, LO C L, CHEN H H, *et al*. Photothermal/NO Combination Therapy from Plasmonic Hybrid Nanotherapeutics Against Breast Cancer[J]. *J Control Release*, 2022, **345**: 417−432. DOI: 10.1016/j.jconrel.2022.03.030.

[18] SHI W Q, HAN Q R, WU J J, *et al*. Synthesis Mechanisms, Structural Models, and Photothermal Therapy Applications of Top-down Carbon Dots from Carbon Powder, Graphite, Graphene, and Carbon Nanotubes[J]. *Int J Mol Sci*, 2022, **23**(3): 1456. DOI: 10.3390/ijms23031456.

[19] CAI K, ZHANG W Y, FODA M F, *et al*. Miniature Hollow Gold Nanorods with Enhanced Effect for in Vivo Photoacoustic Imaging in the NIR-II Window[J]. *Small*, 2020, **16**(37): e2002748. DOI: 10.1002/smll.202002748.

[20] BAO C C, CONDE J, POLO E, *et al*. A Promising Road with Challenges: Where are Gold Nanoparticles in Translational Research? [J]. *Nanomedicine*, 2014, **9**(15): 2353−2370. DOI: 10.2217/nnm.14.155.

[21] DAY E S, ZHANG L N, THOMPSON P A, *et al*. Vascular-targeted Photothermal Therapy of an Orthotopic Murine Glioma Model[J]. *Nanomedicine*, 2012, **7**(8): 1133−1148. DOI: 10.2217/nnm.11.189.

[22] HE S Y, LI J Y, CHEN M J, *et al*. Graphene Oxide-template Gold Nanosheets as Highly Efficient Near-infrared Hyperthermia Agents for Cancer Therapy[J]. *Int J Nanomedicine*, 2020, **15**: 8451−8463. DOI: 10.2147/IJN.S265134.

[23] YIM W, ZHOU J J, MANTRI Y, *et al*. Gold Nanorod-melanin Hybrids for Enhanced and Prolonged Photoacoustic Imaging in the Near-infrared-II Window[J]. *ACS Appl Mater Interfaces*, 2021, **13**(13): 14974−14984. DOI: 10.1021/acsami.1c00993.

[24] MANTRI Y, JOKERST J V. Engineering Plasmonic Nanoparticles for Enhanced Photoacoustic Imaging[J]. *ACS Nano*, 2020, **14**(8): 9408−9422. DOI: 10.1021/acsnano.0c05215.

[25] GE X G, FU Q R, SU L C, *et al*. Light-activated Gold Nanorod Vesicles with NIR-II Fluorescence and Photoacoustic Imaging Performances for Cancer Theranostics [J]. *Theranostics*, 2020, **10**(11): 4809−4821. DOI: 10.7150/thno.44376.

[26] ROACH L, BOOTH M E, INGRAM N, *et al*. Evaluating Phospholipid-functionalized Gold Nanorods for in Vivo Applications[J]. *Small*, 2021, **17**(13): e2006797. DOI: 10.1002/smll.202006797.

[27] TANG H L, XU X J, CHEN Y X, *et al*. Reprogramming the Tumor Microenvironment through Second-near-infrared-window Photothermal Genome Editing of PD-L1 Mediated by Supramolecular Gold Nanorods for En-

hanced Cancer Immunotherapy[J]. *Adv Mater*, 2021, **33**(12): e2006003. DOI: 10.1002/adma.202006003.

[28] SALAZAR SANDOVAL S, CORTÉS-ADASME E, GALLARDO-TOLEDO E, *et al*. B-cyclodextrin-based Nanosponges Inclusion Compounds Associated with Gold Nanorods for Potential NIR-II Drug Delivery[J]. *Pharmaceutics*, 2022, **14**(10): 2206. DOI: 10.3390/pharmaceutics14102206.

[29] LI X J, ZHOU J J, DONG X N, *et al*. In Vitro and in Vivo Photothermal Cancer Therapeutic Effects of Gold Nanorods Modified with Mushroom B-glucan[J]. *J Agric Food Chem*, 2018, **66**(16): 4091−4098. DOI: 10.1021/acs.jafc.8b00292.

[30] DAI X L, LI X, DU Y Y, *et al*. Gold Nanorod–Mesoporous Silica Core Shell Nanocomposites for NIR-II Photothermal Ablation and Dual PD-L1/VEGF Blockade Therapy in Hepatocellular Carcinoma[J]. *Chem Eng J*, 2023, **459**: 141426. DOI: 10.1016/j.cej.2023.141426.

[31] LEBEPE T C, PARANI S, MALULEKE R, *et al*. NIR-II Window Absorbing Graphene Oxide-coated Gold Nanorods and Graphene Quantum Dot-coupled Gold Nanorods for Photothermal Cancer Therapy[J]. *Nanotechnol Rev*, 2023, **12**(1): 20220541. DOI: 10.1515/ntrev-2022-0541.

[32] HE T, JIANG C, HE J, *et al*. Manganese-dioxide-coating-instructed Plasmonic Modulation of Gold Nanorods for Activatable Duplex-imaging-guided NIR-II Photothermal-chemodynamic Therapy[J]. *Adv Mater*, 2021, **33**(13): e2008540. DOI: 10.1002/adma.202008540.

[33] MAHMOUD N N, ABU-DAHAB R, HAMADNEH L A, *et al*. Insights into the Cellular Uptake, Cytotoxicity, and Cellular Death Modality of Phospholipid-coated Gold Nanorods Toward Breast Cancer Cell Lines[J]. *Mol Pharm*, 2019, **16**(10): 4149−4164. DOI: 10.1021/acs.molpharmaceut.9b00470.

[34] WANG X F, MEI Z, WANG Y Y, *et al*. Comparison of Four Methods for the Biofunctionalization of Gold Nanorods by the Introduction of Sulfhydryl Groups to Antibodies[J]. *Beilstein J Nanotechnol*, 2017, **8**: 372−380. DOI: 10.3762/bjnano.8.39.

[35] WANG F, MEN X J, CHEN H B, *et al*. Second Near-infrared Photoactivatable Biocompatible Polymer Nanoparticles for Effective in Vitro and in Vivo Cancer Theranostics[J]. *Nanoscale*, 2021, **13**(31): 13410−13420. DOI: 10.1039/d1nr03156b.

[36] JIANG Y, LI J, ZHEN X, *et al*. Dual-peak Absorbing Semiconducting Copolymer Nanoparticles for First and Second Near-infrared Window Photothermal Therapy: A Comparative Study[J]. *Adv Mater*, 2018, **30**(14): 1705980. DOI:10.1002/adma.201705980.

[37] CHEN Y S, ZHAO Y, YOON S J, *et al*. Miniature Gold Nanorods for Photoacoustic Molecular Imaging in the Second Near-infrared Optical Window[J]. *Nat Nanotechnol*, 2019, **14**(5): 465−472. DOI: 10.1038/s41565-019-0392-3.

[38] SAHU B K, DWIVEDI A, PAL K K, *et al*. Optimized Au NRs for Efficient SERS and SERRS Performances with Molecular and Longitudinal Surface Plasmon Resonance[J]. *Appl Surf Sci*, 2021, **537**: 147615. DOI: 10.1016/j.apsusc.2020.147615.